Matteo Porro
Center for Nano Science and Technology @PoliMi
Istituto Italiano di Tecnologia
Milano
Italy

Dipartimento di Matematica “F. Brioschi”
Politecnico di Milano
Milano
Italy

Carlo de Falco
MOX Modeling and Scientific Computing, Dipartimento di Matematica Politecnico di Milano
Milano
Italy

Centro Europeo di Nanomedicina
Milano
Italy

Maurizio Verri
Dipartimento di Matematica “F. Brioschi”
Politecnico di Milano
Milano
Italy

Guglielmo Lanzani
Center for Nano Science and Technology @PoliMi
Istituto Italiano di Tecnologia
Milano
Italy

Dipartimento di Fisica
Politecnico di Milano
Milano
Italy

Riccardo Sacco
Dipartimento di Matematica “F. Brioschi” Politecnico di Milano
Milano
Italy

Corresponding author : Matteo Porro

Corresponding Author’s Email: matteo.porro@mail.polimi.it

MULTISCALE SIMULATION OF ORGANIC HETEROJUNCTION LIGHT HARVESTING DEVICES

1. Introduction and Motivation. Organic PhotoVoltaic (OPV) devices are usually built by combining a high electronic affinity material (acceptor) with a low electronic affinity material (donor) into a heterojunction structure which may be either highly disordered as is the case, for example, of bulk heterojunction devices, or rather orderly arranged as is the case of bilayer or nanostructured devices (Coakley and McGehee 2004, Mayer, Scully, Hardin, Rowell and McGehee 2007). For the latter two classes of devices it is especially important, in order to properly model the device behaviour, to correctly account for charge generation-recombination phenomena occurring at the interface between the two constituent materials as well as for the nanodipoles associated with charge transfer states which are localized at the same interface. In this direction, a lot of effort has been devoted to developing mathematical models for the simulation of OPV devices that combine a continuum representation of charge transport and diffusion of excited states in bulk materials with an *ad-hoc* description of phenomena occurring at the interfaces (Barker, Ramsdale and Greenham 2003, Ruhstaller, Beierlein, Riel, Karg, Scott and Riess 2003, Williams and Walker 2008, Hwang, McNeill and Greenham 2009, Hausermann, Knapp, Moos, Reinke, Flatz and Ruhstaller 2009, Christ, Kettlitz, Valouch, Zufle, Gartner, Punke and Lemmer 2009, de Falco, Sacco and Verri 2010, de Falco, Iacchetti, Binda, Natali, Sacco and Verri 2011, Neukom, Züfle and Ruhstaller 2012, Brinkman 2013, Brinkman, Fellner, Markowich and Wolfram 2013). In our recent work (de Falco, Porro, Sacco and Verri 2012) we pursued the same goal by means of a multiscale approach, resulting in a model consisting of a coupled system of nonlinear Partial and Ordinary Differential Equations (PDEs/ODEs). For the solution of this model we also proposed a numerical solution algorithm based on Rothe's method and variable-order BDF formulas for time discretization, a Newton linearization and exponentially fitted finite elements for spatial discretization, which was applied to the simulation of nanostructured Organic Solar Cells (OSCs).

In the present paper we adapt and extend the model and methods of (de Falco et al. 2012) to the study of the Light Harvesting Capacitor (LHC) introduced in (Garbugli, Porro, Roiati, Rizzo, Gigli, Petrozza and Lanzani 2012) which is a device exploiting an approach to convert

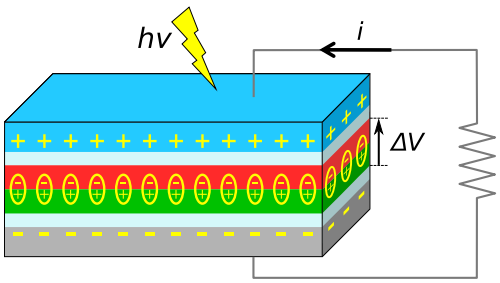

FIG. 2.1. *Scheme of the LHC device and its working principles.*

light energy into electrical energy without generating a steady state charge carrier current through the organic semiconductor materials.
A brief outline of the article is as follows. In Sect. 2 we illustrate the structure and the working principles of the LHC, while in Sects. 3 and 4 we describe the mathematical model. In particular, Sect. 3 deals with the PDE model of a generic donor-acceptor heterostructure while in Sect. 4 we specialize the boundary conditions to the case of the LHC and describe the lumped model used to treat the external circuit. Sect. 5 is devoted to a short description of the computational schemes adopted for model numerical approximation. Sect. 6 contains a description of the performed numerical simulations, a discussion of the obtained results and a list of possible future research perspectives.

2. Light Harvesting Capacitor. The simplest configuration of a LHC, a stack of layers of different materials sandwiched between two electrodes, is schematically represented in Fig. 2.1. Its photoactive compound is made of a double layer of electron donor (D) and acceptor (A) materials, e.g. copper phthalocyanine (CuPc) or metal-free phthalocyanine (H_2Pc) and buckminsterfullerene (C_{60}) or 3,4,9,10-perylenetetracarboxylic bisbenzimidazole (PTCBI), each having a thickness of the order of the exciton diffusion length, few tenths of nanometers. The D-A bilayer is sandwiched between two external layers of optically transparent insulator which confine free charges in the D-A region. Top and bottom electrodes are typically made of indium tin oxide or gold.
The sequence of phenomena that determine the working principles of a LHC are reported in the flowchart of Fig. 2.2. Similarly to what occurs in an OSC, under illumination upon photon absorption, excited states called excitons are formed. These states, which consist in an electron-hole pair and hence have zero net charge, can migrate under the action of diffusive forces towards the material interface before undergoing into decay, typically with characteristic times of few nanoseconds. At the interface between the donor and acceptor materials, the excitons are trapped and form more stable states called bonded pairs. Due to the different

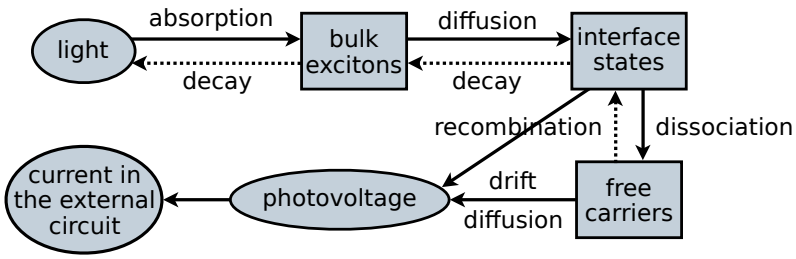

FIG. 2.2. *Flowchart of the phenomena occurring in the active layer of a LHC.*

electronic affinity of the materials, the electron and hole parts of the bonded pairs localize on the acceptor and donor sides of the interface, forming a surface distribution of dipoles. These interface states can then dissociate into free charges that can migrate in the materials by diffusion events and electric field driven drift. Still each of these couples of charges that were used to be bonded together can be seen as a dipole with a larger length, because the insulator layers prevent charge extraction from the electrodes and force the carriers to stay in the D-A bilayer. As a result of this process a macroscopic polarization is induced by the coherent sum of the photoinduced oriented nanodipoles, due to the particular ordered planar structure of the device. As a consequence, the capacitor plates that sandwich in between the polarized medium, allow harvesting the electrochemical potential stored in the collective charge separated state, giving rise to a transient current in the external circuit that can be used to generate power through a load resistance. In this manner one can convert light energy into electrical energy without generating a steady state charge carrier current through the active layer, maintaining at the same time internal quantum efficiency high since no transport issues have to be faced. When illumination is stopped, the polarization decays causing a second transient current flow, in opposite direction, through the external load, hence allowing for further energy extraction. In principle, since charge transport is not an issue, it would be beneficial for the device performace to stack a large number of layers in order to fully exploit the available amount of energy in the incident light, possibly using different materials in each layer of the stack to cover the largest possible radiation spectrum (Garbugli et al. 2012).

3. Mathematical Model. In this section we illustrate the PDE/ODE mathematical model accounting for excitation phenomena, interface charge state evolution and photogenerated charge transport occurring in the bulk of a LHC device like that of Fig. 2.1. The model was introduced in (de Falco et al. 2012) and represents a multi-dimensional generalization of the 1D formulation proposed in (Barker et al. 2003).
Throughout the section, we denote by Ω an open subset of $\mathbb{R}^d$, $d = 1, 2, 3$, that represents the geometrical model of the bulk of a generic heterostructure OPV device. The boundary of the domain is $\partial\Omega$ and $\boldsymbol{\nu}$ is the unit outward normal vector over $\partial\Omega$. Fig. 3.1 shows an example of the computational domain Ω in the 2D case.
The device structure is divided into two open disjoint subregions, Ω_n and Ω_p, representing the domains occupied by the acceptor and donor phases, respectively, with Γ_{C} and Γ_{A} denoting the cathode and anode contacts, respectively. The acceptor and donor regions are separated by a regular surface Γ, representing an intermixing interface region, on which a unit normal vector $\boldsymbol{\nu}_\Gamma$ is defined, oriented from Ω_p into Ω_n. For any function $f : \Omega \to \mathbb{R}$, the *jump* of f across Γ is defined as $[\![f]\!] := f_n - f_p$, f_n and f_p being the traces of f on Γ from the interior of Ω_n and Ω_p, respectively.

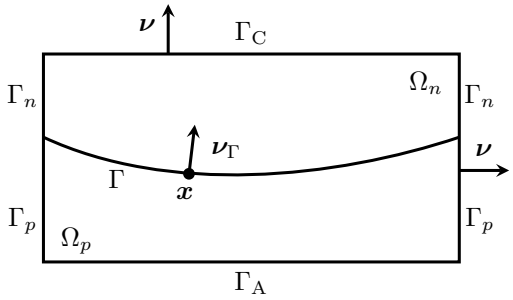

FIG. 3.1. *Geometry of an OPV device and mathematical notation.*

From now on, the problem dependent variables X, n and p denote the volumetric densities of excitons, electrons and holes in the device, respectively, while P and φ are the areal density of bonded pairs and the electric potential, respectively.
Excitation phenomena occurring in the bulk as a consequence of light absorption are described by the parabolic problem:

$$\begin{cases} \dfrac{\partial X}{\partial t} + \nabla \cdot \mathbf{J}_X = G - \dfrac{X}{\tau_X} & \text{in } \Omega \setminus \Gamma, \\ \mathbf{J}_X = -D_X \nabla X & \text{in } \Omega \setminus \Gamma, \\ [\![X]\!] = 0 & \text{on } \Gamma, \\ [\![-\boldsymbol{\nu}_\Gamma \cdot \mathbf{J}_X]\!] = \eta k_{\mathrm{rec}} P - \dfrac{2H}{\tau_{\mathrm{diss}}} X & \text{on } \Gamma, \\ -\kappa_X \, \boldsymbol{\nu} \cdot \mathbf{J}_X + \alpha_X X = \beta_X & \text{on } \Gamma_{\mathrm{C}} \cup \Gamma_{\mathrm{A}}, \\ X(\boldsymbol{x}, 0) = 0 & \forall \boldsymbol{x} \in \Omega. \end{cases} \tag{3.1a}$$

The first two equations in (3.1a) represent the time rate of change of exciton number density in the bulk of the LHC due to the balance between net diffusive flux ($\nabla \cdot \mathbf{J}_X$), sources (optical generation rate, G) and sinks (decay rate, $-X/\tau_X$). The first interface equation ($[\![X]\!] = 0$) expresses exciton density continuity across the surface Γ. The second interface equation has the same meaning as the first two equations in (3.1a) and expresses the balance between the net exciton diffusive flux across the active layer thickness ($[\![-\boldsymbol{\nu}_\Gamma \cdot \mathbf{J}_X]\!]$), sources (exciton production due to interface state recombination events, $\eta k_{\mathrm{rec}} P$) and sinks (rate of transition from exciton to bonded pair state, $-2HX/\tau_{\mathrm{diss}}$). We note that this latter transition is assumed to be instantaneous in other studies (Barker et al. 2003, Williams and Walker 2008, Williams 2008). Finally, the last two equations in (3.1a) are boundary and initial conditions in the device. The boundary conditions express once again a balance at the two contacts between injection current flux and net recombination phenomena. The initial condition simply states that before switching the device into the on state, the bulk is completely depleted of excitons.
The evolution of bonded pairs at the material interface, accounting for the dissociation and decay events involving excitons and free charge carriers, is described by the ODE:

$$\begin{cases} \dfrac{\partial P}{\partial t} = \dfrac{2H}{\tau_{\mathrm{diss}}} X + 2H\gamma np - \left(k_{\mathrm{diss}} + k_{\mathrm{rec}}\right) P & \text{on } \Gamma, \\ P(\boldsymbol{x}, 0) = 0 & \forall \boldsymbol{x} \in \Gamma. \end{cases} \tag{3.1b}$$

The first equation in (3.1b) represents the time rate of change of polaron number density in the active layer thickness due to the balance between sources (exciton dissociation, $2HX/\tau_{\mathrm{diss}}$, and bimolecular recombination, $2H\gamma np$) and sinks (polaron dissociation and recombination, $-\left(k_{\mathrm{diss}} + k_{\mathrm{rec}}\right) P$). The initial condition is the same as that for excitons.
Transport of photogenerated electrons in the acceptor domain Ω_n is described by the parabolic problem:

$$\begin{cases} \dfrac{\partial n}{\partial t} + \nabla \cdot \mathbf{J}_n = 0 & \text{in } \Omega_n, \\ \mathbf{J}_n = -D_n \nabla n + \mu_n n \nabla \varphi & \text{in } \Omega_n, \\ -\boldsymbol{\nu}_\Gamma \cdot \mathbf{J}_n = -k_{\mathrm{diss}} P + 2H\gamma np & \text{on } \Gamma, \\ -\kappa_n \, \boldsymbol{\nu} \cdot \mathbf{J}_n + \alpha_n n = \beta_n & \text{on } \Gamma_{\mathrm{C}}, \\ n(\boldsymbol{x}, 0) = 0 & \forall \boldsymbol{x} \in \Omega. \end{cases} \tag{3.1c}$$

The first two equations in (3.1c) represent the classical continuity equation for electrons in the drift-diffusion model. The boundary condition at the cathode electrode has the same meaning as that for excitons and a similar comment applies to the interface condition across Γ and to the initial condition. A parabolic problem completely similar to (3.1c) describes hole transport in the donor domain Ω_p.
The dependence of the electric potential and field on the space charge density in the device is described by the Poisson problem:

$$\begin{cases} \nabla \cdot \mathbf{D} = -q\, n & \text{in } \Omega_n, \\ \nabla \cdot \mathbf{D} = +q\, p & \text{in } \Omega_p, \\ \mathbf{D} = -\varepsilon \nabla \varphi & \text{in } \Omega, \\ [\![-\boldsymbol{\nu}_\Gamma \cdot \mathbf{D}]\!] = 0 & \text{on } \Gamma, \\ [\![\varphi]\!] = -\dfrac{qdP}{\varepsilon^*} & \text{on } \Gamma, \\ -\kappa_\varphi\, \boldsymbol{\nu} \cdot \mathbf{D} + \alpha_\varphi \varphi = \beta_\varphi & \text{on } \Gamma_{\mathrm{C}} \cup \Gamma_{\mathrm{A}}, \end{cases} \tag{3.1d}$$

where $\mathbf{D}$ is the electric displacement vector and q is the elementary charge. System (3.1d) expresses Gauss' law in differential form in the various regions of the device, with proper coupling interface conditions across the interface Γ. The first of these conditions is the usual compatibility condition for the displacement vector arising in Maxwell's equation theory, while the second condition is a novel contribution of the present model compared to that proposed in (de Falco et al. 2012). The jump term for the electric potential at the D-A interface Γ accounts for the effect of the dipoles of the bonded pairs and physically represents the voltage drop across a capacitor with a surface charge qP on its plates and capacitance per unit area ε^*/d, d being the electron-hole separation length in the bonded pairs and ε^* being the harmonic average of the values of the dielectric permittivity on the two sides of the interface. The form of the boundary conditions on Γ_{A} and Γ_{C} depends on the specific configuration of the external circuit connected to the device.
System (3.1) is completed by periodic boundary conditions on $\Gamma_n \cup \Gamma_p$. A list of the model parameters with their corresponding physical meaning is reported in Table 3.1.
We notice that the dissociation and recombination processes occurring at the donor-acceptor interface Γ are dealt with by the nonlinear transmission conditions $(3.1\mathrm{a})_3$ and $(3.1\mathrm{c})_2$, whose dependence on the local electric field magnitude and orientation is contained in the bonded pair dissociation rate constant k_{diss}. This latter coefficient is modeled according to the approach proposed in (de Falco et al. 2012), which in the present 1D setting turns out to coincide with that of (Barker et al. 2003).
For the physical models of the remaining coefficients in system (3.1) we refer to (Barker et al. 2003, Gill 1972, Horowitz 1998). In particular, for the carrier mobilities, we neglect the effect of energetic disorder, so that they can be assumed to depend only on the electric field magnitude, according to the Poole-Frenkel model. As for diffusivities, in the computations of Sect. 6, Einstein relations

$$D_n = (K_B T/q)\mu_n, \qquad D_p = (K_B T/q)\mu_p \tag{3.2}$$

are assumed to hold, although the proposed multiscale formulation remains unchanged if such an assumption is removed. In (3.2), K_{B} is Boltzmann's constant and T is the absolute temperature.
Regarding the bimolecular recombination rate constant γ the Langevin-type relation presented in (Barker et al. 2003) is used with a small modification motivated by the fact that

TABLE 3.1
Model parameters.

Symbol	Parameter
μ_i, D_i	Mobility and diffusivity of species i, $i = X, n, p$
G	Exciton generation rate
τ_X, $\tau_{\rm diss}$	Exciton decay and dissociation times
$k_{\rm rec}$, $k_{\rm diss}$	Bonded pair recombination and dissociation rate constants
γ	Electron-hole recombination rate constant
η	Singlet exciton fraction
H	Active layer thickness
ε	Dielectric permittivity

the original model has been observed to lead to a systematic overestimation of the amount of recombination occurring at the interface. Therefore, we employed the following expression

$$\gamma = \zeta \frac{q\mu_{\rm min}}{3\varepsilon^*}, \tag{3.3}$$

where μ_{min} denotes the minimum of the carrier mobilities at the interface. In (3.3) we introduced the non-dimensional fitting parameter ζ which in Sect. 6 was set to $\zeta = .3$ to correctly capture the off-state transient behaviour of the device. The physical understanding of this overestimation of the recombination term is as of yet not complete and deserves further investigation.

Other modeling approaches similar to that of the present article, but applied to OSCs, have been proposed in the recent literature. In (Hausermann et al. 2009, Hwang et al. 2009, Christ et al. 2009) a drift-diffusion analysis of bulk-heterojunction OSCs is carried out, including dissociation of charge-transfer exciton, transient photocurrent simulations and a sensitivity analysis. In (Neukom et al. 2012) a model parameter fitting for OSCs is performed using multiple experimental data sets and a thorough parameter correlation analysis.

4. Application to the LHC. Fig. 4.1 illustrates a schematical representation of the LHC of Fig. 2.1, where the geometrical notation used for the bulk region is in accordance with that used in Sect. 3. The quantities $C_{\rm C}$ and $C_{\rm A}$ are the geometric capacitances of the dielectric layers in contact with cathode and anode respectively, R is the resistive load connected to the device and the voltage source $V_{\rm BI}$ represents the device built-in potential due to the difference in the work functions of the contact materials. Given the planar structure of the device shown in Fig. 2.1, the simulations discussed in Sect. 6 are performed in the 1D geometry schematically represented in Fig. 4.2. We assume the cathode to be in the origin of the reference system and with $L_{\rm ox,l}$ and $L_{\rm ox,r}$ we refer to the thicknesses of the left and right dielectric layers while with $L_{\rm acc}$ and $L_{\rm don}$ we denote those of the acceptor and donor materials, respectively.

The presence of the insulating layers and of the external circuit depicted in Fig. 4.1 is ac-

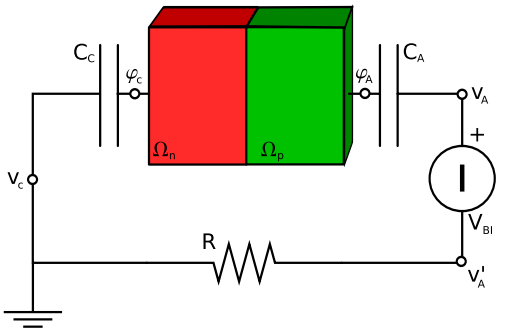

FIG. 4.1. *Circuit representation of a LHC.*

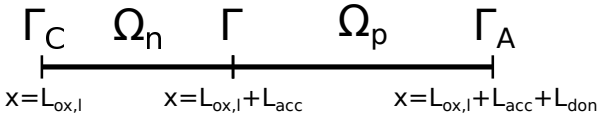

FIG. 4.2. *1D computational domain for the LHC simulation.*

counted for in the model (3.1) by the following set of boundary conditions:

$$\begin{cases} -\boldsymbol{\nu}\cdot\mathbf{J}_X = 0 & \text{on } \Gamma_{\mathrm{C}}\cup\Gamma_{\mathrm{A}}, \\ -\boldsymbol{\nu}\cdot\mathbf{J}_n = 0 & \text{on } \Gamma_{\mathrm{C}}, \\ -\boldsymbol{\nu}\cdot\mathbf{J}_p = 0 & \text{on } \Gamma_{\mathrm{A}}, \\ -\boldsymbol{\nu}\cdot\mathbf{D} = \dfrac{C_{\mathrm{C}}}{S}\left(\mathrm{v}_{\mathrm{C}}-\varphi\right) & \text{on } \Gamma_{\mathrm{C}}, \\ -\boldsymbol{\nu}\cdot\mathbf{D} = \dfrac{C_{\mathrm{A}}}{S}\left(\mathrm{v}_{\mathrm{A}}-\varphi\right) = \dfrac{C_{\mathrm{A}}}{S}\left(\mathrm{v}'_{\mathrm{A}}+V_{\mathrm{BI}}-\varphi\right) & \text{on } \Gamma_{\mathrm{A}}, \\ \dfrac{\mathrm{v}'_{\mathrm{A}}-\mathrm{v}_{\mathrm{C}}}{R} = \dfrac{C_{\mathrm{A}}}{S}\dfrac{\partial}{\partial t}\left(\varphi_{\mathrm{A}}-\mathrm{v}_A\right) = \dfrac{C_{\mathrm{C}}}{S}\dfrac{\partial}{\partial t}\left(\mathrm{v}_{\mathrm{C}}-\varphi_{\mathrm{C}}\right) & \end{cases} \tag{4.1}$$

where S is the cross-sectional area of the LHC in the plane perpendicular to the x-axis in Fig. 4.2. Conditions $(4.1)_1$-$(4.1)_3$ state that at the interfaces with the insulating layers no exciton quenching occurs and that free charges are confined in the D-A region. Conditions $(4.1)_4$-$(4.1)_5$, instead, represent the conservation of the normal component of the displacement field at Γ_{C} and Γ_{A} while Kirchhoff's law $(4.1)_6$ closes the system by introducing the coupling with the external circuit. The boundary conditions (4.1) fit into the general framework of (3.1) upon setting:

$$\begin{cases} \alpha_X = \beta_X = 0, \ \ \kappa_X = 1 & \text{on } \Gamma_{\mathrm{C}}\cup\Gamma_{\mathrm{A}}, \\ \alpha_n = \beta_n = 0, \ \ \kappa_n = 1 & \text{on } \Gamma_{\mathrm{C}}, \\ \alpha_p = \beta_p = 0, \ \ \kappa_p = 1 & \text{on } \Gamma_{\mathrm{A}}, \\ \alpha_\varphi = \dfrac{C_{\mathrm{C}}}{S}, \ \ \beta_\varphi = \mathrm{v}_{\mathrm{C}}\dfrac{C_{\mathrm{C}}}{S}, \ \ \kappa_\varphi = 1 & \text{on } \Gamma_{\mathrm{C}}, \\ \alpha_\varphi = \dfrac{C_{\mathrm{A}}}{S} \quad , \beta_\varphi = \left(\mathrm{v}'_{\mathrm{A}}+V_{\mathrm{BI}}\right)\dfrac{C_{\mathrm{A}}}{S}, \ \ \kappa_\varphi = 1 & \text{on } \Gamma_{\mathrm{A}}. \end{cases} \tag{4.2}$$

We conclude this section by describing the model for the exciton generation rate term G. Since light absorption is a crucial aspect of the working principles of a LHC, especially in the configuration where several D-A bilayers are stacked, it is mandatory to adopt an appropriate model which takes into account progressive absorption in the materials. For this reason we consider the Beer-Lambert model which, under the hypothesis that light hits the device from the cathode, in the considered computational domain of Fig. 4.2 reads:

$$G(x,t) = \begin{cases} \alpha_{\rm acc} I_0(t)\, e^{-\alpha_{\rm acc}(x - L_{\rm ox,1})} & x \in \Omega_n \\ \alpha_{\rm don} I_\Gamma(t)\, e^{-\alpha_{\rm don}(x - L_{\rm ox,1} - L_{\rm acc})} & x \in \Omega_p \end{cases} \tag{4.3}$$

where $\alpha_{\rm acc}$ and $\alpha_{\rm don}$ are the absorption coefficients of t heacceptor a nddonor materials, $I_0(t)$ is the photon incidence rate per area and $I_\Gamma(t) = I_0(t)\ \left(1 - e^{-\alpha_{\rm acc} L_{\rm acc}}\right)$ is the value of I_0 at the interface Γ at time t.
It should be noted that more complex optical models are available in the literature for the simulation of light-harvesting organic semiconductor devices, e.g. those based on the transfer matrix approach (Hausermann et al. 2009, Hwang et al. 2009, Christ et al. 2009). Nevertheless in the current work we do not intend to investigate in detail such aspect and we consider the Beer-Lambert model to be accurate enough for our scope, leaving the inclusion of such feature for future activities.

5. Numerical Methods. System linearization (by a quasi-Newton method) and approximation are carried out by adapting the approach used in (de Falco et al. 2010) and in (de Falco et al. 2012) to which we refer for all implementation details. Time advancing is treated using Rothe's method and adaptive BDF formulas, while the exponentially fitted Galerkin finite element method studied in (Gatti, Micheletti and Sacco 1998) is used for spatial discretization. The interface conditions at the donor-acceptor interface are taken care of by means of the substructuring techniques described in (Hughes, Engel, Mazzei and Larson 2000).

6. Numerical simulation results. We start our numerical study with a validation of the predictions of the proposed model by comparison with experimental measurements carried out on a prototype LHC device presented in (Garbugli et al. 2012). Such a device consists of a multilayer structure of ITO/PMMA $(100\,\mathrm{nm})$/PTCBI $(40\,\mathrm{nm})$/H_2Pc $(20\,\mathrm{nm})$/PMMA $(100\,\mathrm{nm})$/Gold and a load of resistance $R = 1\,\mathrm{M\Omega}$ is connected to the electrodes. The device is illuminated from the ITO side with a monochromatic source at $632\,\mathrm{nm}$ with $40\,\mathrm{mW\,cm^{-2}}$ power density for $40\,\mathrm{ms}$ and then the light is switched off letting the system evolve to a rest state. The output measure of the experiment is the photogenerated current that flows in the external circuit across the load. The choice of gold as the material for the reflective electrode has been made to minimize the effects due to a built-in voltage resulting from different electrode materials. For this reason, from now on we assume gold to have the same work function as ITO and hence $V_{\rm BI} = 0\,\mathrm{V}$. Other geometrical parameters and material properties of the simulated device are listed in Table 6. Since some of these values are known just up to a certain level of uncertainty, some fitting operations have been performed in order to better match the experimental measures with the simulation results.
Fig. 6.1 shows the measured current for the LHC studied in (Garbugli et al. 2012) (blue solid line), the illumination input signal (black dotted line) and the simulated dynamics obtained with the model proposed in this work (red). We notice an excellent agreement between simulation and measurements, in particular, both the positive and negative current peaks following the light turn on-off switching are accurately captured, with similar intensities and characteristic times.
In order to investigate in more detail the inner working principles of the LHC we proceed in the following by discussing in detail the evolution of the quantities that appear in model (3.1)-

TABLE 6.1
Model parameters obtained after the fitting procedure.

Parameter	**Symbol**	**Unit**	**Fitted Value**
Device Area	S	mm^2	25
Load	R	Ω	10^6
PTCBI relative permittivity	ε	-	4.5
H_2PC relative permittivity	ε	-	4
PMMA relative permittivity	ε	-	4
PTCBI zero-field mobility	$\mu_{n,0}$	$\mathrm{cm}^2\,\mathrm{V}^{-1}\,\mathrm{s}^{-1}$	10^{-5}
H_2PC zero-field mobility	$\mu_{p,0}$	$\mathrm{cm}^2\,\mathrm{V}^{-1}\,\mathrm{s}^{-1}$	10^{-5}
PTCBI field-dependence mobility parameter	γ_n	$\mathrm{cm}^{1/2}\,\mathrm{V}^{-1/2}$	10^{-3}
H_2PC field-dependence mobility parameter	γ_p	$\mathrm{cm}^{1/2}\,\mathrm{V}^{-1/2}$	10^{-3}
Exciton diffusivity	D_X	$\mathrm{cm}^2\,\mathrm{s}^{-1}$	10^{-3}
Active layer half-thickness	H	m	10^{-9}
Dipole length	d	m	$2 \cdot 10^{-9}$
Exciton life time	τ_X	s	10^{-9}
Exciton dissociation time	τ_{diss}	s	10^{-12}
Bonded pair dissociation zero-field rate constant	$k_{\mathrm{diss},0}$	s^{-1}	10^7
Bonded pair recombination rate constant	k_{rec}	s^{-1}	10^5
Singlet exciton fraction	η_X	-	0.25
PTCBI absorption parameter	α_n	cm^{-1}	0
H_2PC absorption parameter	α_p	cm^{-1}	$2 \cdot 10^5$

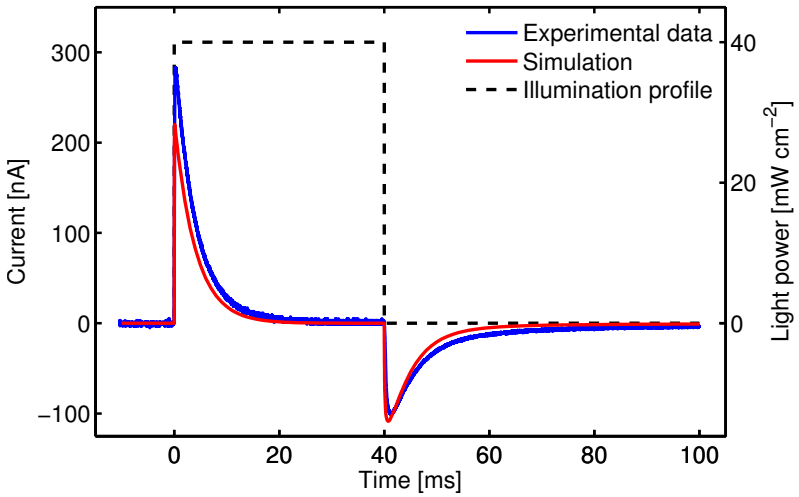

FIG. 6.1. *Experimental data vs. numerical results.*

(4.1) during both the switching on and off transients. In this task, for a more efficient presentations of cause-and-effect relationships, we present the obtained results following the same order of the conceptual scheme of Fig. 2.2.

In Fig. 6.2 we report a sequence of exciton density profiles in the donor side of the device and

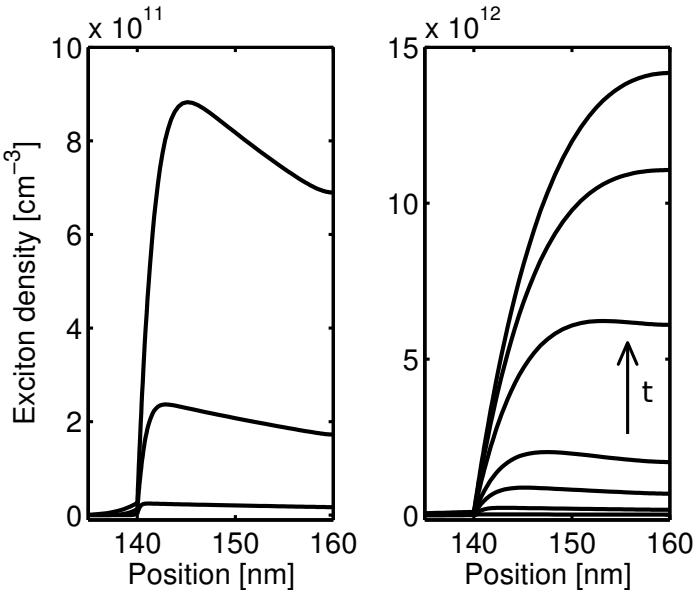

FIG. 6.2. *Computed exciton density in the donor at* $t = 1\,\mathrm{ps}, 10\,\mathrm{ps}, 40\,\mathrm{ps}$ *(left) and at* $t = 1\,\mathrm{ps}, 10\,\mathrm{ps}, 40\,\mathrm{ps}, 100\,\mathrm{ps}, 400\,\mathrm{ps}, 1\,\mathrm{ns}, 10\,\mathrm{ns}$ *(right).*

in a few nanometers of the acceptor closest to the material interface. Since both exciton decay (τ_X) and bonded pair transition (τ_{diss}) characteristic times are very small, exciton dynamics show very fast transients. In the very first picoseconds of the simulation, exciton density clearly resembles the exponential profile of the Beer-Lambert generation term, except for the region close to the interface, where the excited states are rapidly captured, forming the charge transfer states. At later time levels, diffusion and decay phenomena play a more important role and in just about $10\,\mathrm{ns}$ a stationary regime is reached, in which excitons show a smooth profile, see Fig. 6.2 (right).

Since the time scales of the various phenomena occurring during the transients are spread over a wide range, in Fig. 6.1 the current appears to switch instantaneously from zero to a positive value and it is not possible to appreciate its fast dynamics. In order to better analyze this latter, in Fig. 6.3 we show a log-plot of the computed photovoltage $\mathrm{v}'_{\mathrm{A}} - \mathrm{v}_{\mathrm{C}} = Ri$, where i is the current that flows in the external load R, as a function of time. The use of log-scale for the time clarifies the fact that the photovoltage (and hence the current) rises up in a finite time of the order of some hundreds of microseconds, with a smooth transition from the rest state. Moreover this characteristic time scale (highlighted with the dotted line) coincides with that of the bonded pairs dynamics also reported in Fig. 6.3 with the red line. In fact, the photovoltage is a result of the generation of bonded pairs and free carriers and when these latter reach an equilibrium, it cannot increase anymore. Since in the considered case the resistive load is relatively big, the external circuit dynamics is quite slow and does not interfere with the developed photovoltage. For longer time scales, the displacement current starts to play a major role in reducing the photovoltage, by giving rise to an electric field which acts against that generated by the bonded pairs and the free charges in the donor and acceptor phases.

In Fig. 6.4 we report the computed electron and hole densities in both the acceptor and donor material at selected time levels. As we already pointed out, the characteristic time scale of the evolution of charge carriers is remarkably different from that of excitons, hence the selected

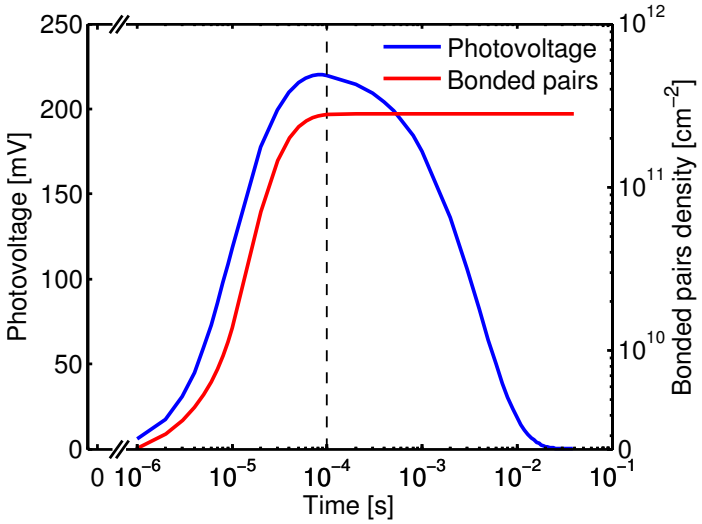

FIG. 6.3. *Semilogarthimic plot of the computed photovoltage and comparison with charge transfer states dynamics at the interface.*

time steps are of the order of microseconds instead of picoseconds. Results show that in the early stages after light switching on, charge carriers tend to migrate from the interface towards the bulk materials under the action of pure diffusion forces, since there is no built-in electric field and free charge densities are too low to determine significant fields. Nevertheless when this charge displacement grows in magnitude, it generates an electric field directed from the donor side to the acceptor one that tends to balance the diffusion effects and to inhibit charge transport away from the interface. As a result of this process, high densities of charge carriers are built-up at the donor-acceptor interface and this in turn enhances the probability of bimolecular recombination events which balance the bonded pair dissociation flux, leading to a stationary situation. For longer times, of the order of the circuit time scale, this steady state configuration undergoes very few modifications by the slight changes in the electric field due to the charge rearrangement on the external electrodes.

To conclude this section we briefly analyze the switching off dynamics of the device. When the incident photon flow is interrupted, the exciton population in the acceptor suddenly drops to almost zero, so that bonded pair formation and recombination are no longer balanced processes. Hence, bonded pair interface density starts to decrease and in this chain of events also a net flux from the free charge state to interface bonded state occurs. In Fig. 6.5 we report the free charge carriers densities for several time levels after the light switching off time. The obtained profiles are qualitatively similar to those observed during the illumination period but the characteristic time scale is several times longer. A possible motivation is the fact that electron-hole recombination is a bimolecular process and hence slower than bonded pair dissociation, which is a monomolecular event, up to electric field dependence effects. As a matter of fact, even if at equilibrium they have the same characteristic rate, when charge carrier densities are reduced, also the recombination characteristic rate is reduced since it depends on them. As a result the discharge process is slower and the displacement current flowing in the external circuit has a longer characteristic time, see Fig. 6.1.

7. Conclusions and Future Work. In the present article, we have proposed a refinement of the model introduced in (Garbugli et al. 2012) for the mathematical and numerical investigation of the dynamical performance of a LHC. The considered formulation is

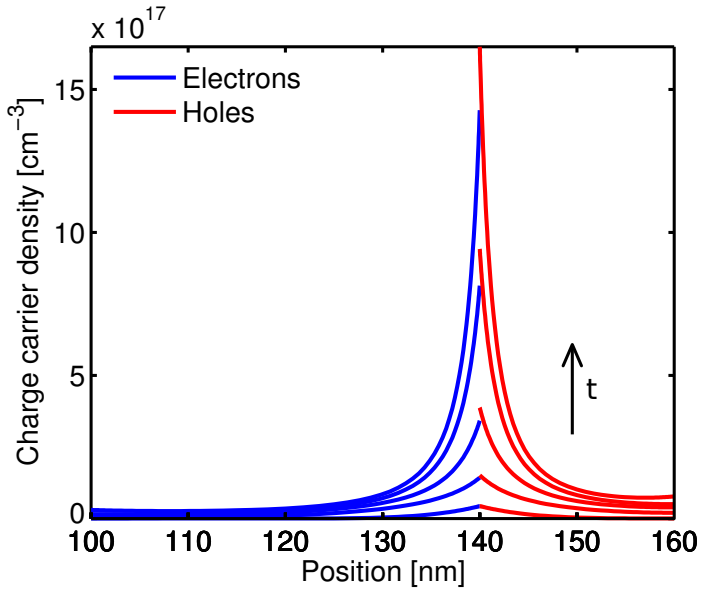

FIG. 6.4. *Computed carrier densities at* $t = 1\,\mu\text{s}, 5\,\mu\text{s}, 10\,\mu\text{s}, 20\,\mu\text{s}, 30\,\text{ms}$.

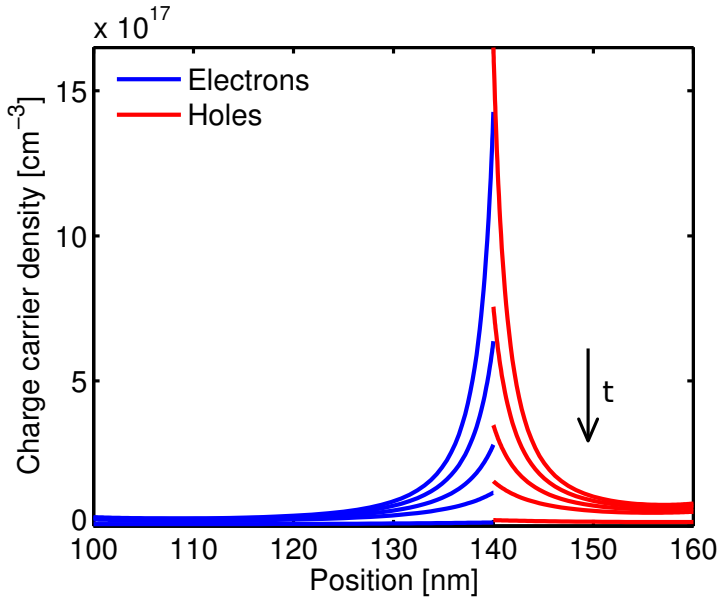

FIG. 6.5. *Computed carrier densities at times* $t = 0\,\text{s}, 50\,\mu\text{s}, 200\,\mu\text{s}, 1\,\text{ms}, 60\,\text{ms}$ *after illumination is switched off.*

an extension of the PDE/ODE system described in (de Falco et al. 2010, de Falco et al. 2011, de Falco et al. 2012).

Simulation results show remarkable agreement with experimentally measured current transients in the device. Moreover, the new enhanced model allows for better insight on the microscopic phenomena which affect the external LHC performance but cannot be directly measured or accurately represented by resorting to a lumped description as in (Garbugli et al.

2012). In particular, the analysis of the obtained results permits to distinguish the wide range of different time scales at which the above mentioned phenomena occur.

However several aspects have not been addressed yet in this work and need to be investigated in the ongoing research activity. Among all we intend to:

1. further validate the model over a larger number of measurements and a wider set of different experiments, in order to strengthen the fitting of the parameters;
2. carry out a sensitivity analysis of the model with respect to its many parameters as well as a parameter correlation analysis, in the same spirit as in (Hausermann et al. 2009, Neukom et al. 2012, de Vries, Badinski, Janssen and Coehoorn 2013);
3. use the predictive power of the model to characterize the maximum potential efficiency of novel LHC devices and to provide indications on the design of device and external circuit for the tuning of the energy conversion efficiency;
4. include in the physical models of the PDE/ODE coefficients higher-order phenomena such as energetic disorder (Pasveer, Cottaar, Tanase, Coehoorn, Bobbert, Blom, De Leeuw and Michels 2005, Knapp, Häusermann, Schwarzenbach and Ruhstaller 2010, Coehoorn and Bobbert 2012, Maddalena, de Falco, Caironi and Natali 2014) and more complex bimolecular recombination processes involving charge trapping states (Koster, Mihailetchi and Blom 2006, Kuik, Koster, Wetzelaer and Blom 2011);

REFERENCES

J. Barker, C. Ramsdale and N. Greenham (2003), 'Modeling the current-voltage characteristics of bilayer polymer photovoltaic devices', *Phys. Rev. B* **67**, 075205.

D. Brinkman (2013), Modeling and numerics for two partial differential equation systems arising from nanoscale physics, PhD thesis, University of Cambridge.

D. Brinkman, K. Fellner, P. A. Markowich and M.-T. Wolfram (2013), 'A drift-diffusion-reaction model for excitonic photovoltaic bilayers: Asymptotic analysis and a 2d hdg finite element scheme', *Mathematical Models and Methods in Applied Sciences* **23**(05), 839–872.

N. S. Christ, S. W. Kettlitz, S. Valouch, S. Zufle, C. Gartner, M. Punke and U. Lemmer (2009), 'Nanosecond response of organic solar cells and photodetectors', *Journal of Applied Physics* **105**(10), 104513.

K. Coakley and M. McGehee (2004), 'Conjugated polymer photovoltaic cells', *Chemistry of Materials* **16**(23), 4533–4542.

R. Coehoorn and P. A. Bobbert (2012), 'Effects of gaussian disorder on charge carrier transport and recombination in organic semiconductors', *physica status solidi (a)* **209**(12), 2354–2377.

C. de Falco, A. Iacchetti, M. Binda, D. Natali, R. Sacco and M. Verri (2011), Modeling and simulation of organic solar cells, in *Scientific Computing in Electrical Engineering SCEE 2010* (B. Michielsen and J.-R. Poirier, eds), Vol. 16 of *Mathematics in Industry*.

C. de Falco, M. Porro, R. Sacco and M. Verri (2012), 'Multiscale modeling and simulation of organic solar cells', *Computer Methods in Applied Mechanics and Engineering* **245–246**, 102 – 116.

C. de Falco, R. Sacco and M. Verri (2010), 'Analytical and numerical study of photocurrent transients in organic polymer solar cells', *Comput. Meth. Appl. Mech. Engrg.* **199**(25-28), 1722 – 1732.

R. J. de Vries, A. Badinski, R. A. J. Janssen and R. Coehoorn (2013), 'Extraction of the materials parameters that determine the mobility in disordered organic semiconductors from the current-voltage characteristics: Accuracy and limitations', *Journal of Applied Physics* **113**(11), 114505.

M. Garbugli, M. Porro, V. Roiati, A. Rizzo, G. Gigli, A. Petrozza and G. Lanzani (2012), 'Light energy harvesting with nano-dipoles', *Nanoscale* **4**, 1728–1733.

E. Gatti, S. Micheletti and R. Sacco (1998), 'A new Galerkin framework for the drift-diffusion equation in semiconductors', *East-West J. Numer. Math.* **6**, 101–136.

W. Gill (1972), 'Drift mobilities in amorphous charge-transfer complexes of trinitrofluorenone and poly-n-vinylcarbazole', *J. Appl. Phys.* **55**(12), 5033.

R. Hausermann, E. Knapp, M. Moos, N. A. Reinke, T. Flatz and B. Ruhstaller (2009), 'Coupled optoelectronic simulation of organic bulk-heterojunction solar cells: Parameter extraction and sensitivity analysis', *Journal of Applied Physics* **106**(10), 104507.

G. Horowitz (1998), 'Organic field-effect transistors', *Advanced Materials* **10**(5), 365–377.

T. Hughes, G. Engel, L. Mazzei and M. Larson (2000), 'The continuous Galerkin method is locally conservative', *J. Comp. Phys.* **163**, 467–488.

I. Hwang, C. R. McNeill and N. C. Greenham (2009), 'Drift-diffusion modeling of photocurrent transients in bulk heterojunction solar cells', *Journal of Applied Physics* **106**(9), 094506.

E. Knapp, R. Häusermann, H. Schwarzenbach and B. Ruhstaller (2010), 'Numerical simulation of charge transport in disordered organic semiconductor devices', *Journal of Applied Physics* **108**, 054504.

L. J. A. Koster, V. D. Mihailetchi and P. W. M. Blom (2006), 'Bimolecular recombination in polymer/fullerene bulk heterojunction solar cells', *Applied Physics Letters* **88**(5), 052104.

M. Kuik, L. J. A. Koster, G. A. H. Wetzelaer and P. W. M. Blom (2011), 'Trap-assisted recombination in disordered organic semiconductors', *Phys. Rev. Lett.* **107**, 256805.

F. Maddalena, C. de Falco, M. Caironi and D. Natali (2014), 'Assessment of the density of states in organic semiconductors', *Physical Review B (submitted)*.

A. Mayer, S. Scully, B. Hardin, M. Rowell and M. McGehee (2007), 'Polymer-based solar cells', *Materials Today* **10**(11), 28–33.

M. Neukom, S. Züfle and B. Ruhstaller (2012), 'Reliable extraction of organic solar cell parameters by combining steady-state and transient techniques', *Organic Electronics* **13**(12), 2910 – 2916.

W. Pasveer, J. Cottaar, C. Tanase, R. Coehoorn, P. Bobbert, P. Blom, D. De Leeuw and M. Michels (2005), 'Unified description of charge-carrier mobilities in disordered semiconducting polymers', *Physical Review Letters* **94**(20), 206601.

B. Ruhstaller, T. Beierlein, H. Riel, S. Karg, J. Scott and W. Riess (2003), 'Simulating electronic and optical processes in multilayer organic light-emitting devices', *Selected Topics in Quantum Electronics, IEEE Journal of* **9**(3), 723–731.

J. Williams (2008), Finite Element Simulations of Excitonic Solar Cells and Organic Light Emitting Diodes, PhD thesis, University of Bath.

J. Williams and A. Walker (2008), 'Two-dimensional simulations of bulk heterojunction solar cell characteristics', *Nanotechnology* **19**, 424011.